



Cite this: *J. Anal. At. Spectrom.*, 2023, **38**, 2113

High spatial resolution (10–50 µm) analysis of Sr isotopes in rock-forming apatite by LA-MC-ICP-MS†

Anda Buzenchi, * Hugo Moreira, Olivier Bruguier, Delphine Bosch and Bruno Dhuime

In situ Sr isotopes analysis of apatite by LA-(MC)-ICP-MS is challenged by the difficulty to monitor and correct isobaric interferences from atomic and polyatomic ions. We present a new routine procedure for analysing rock-forming apatites with a Thermo Scientific Neptune XT MC-ICP-MS coupled with a Teledyne Cetac Analyte Excite+ 193 nm laser ablation system. Five apatite standards that cover a large range of REE/Sr ratios were selected, and their $^{87}\text{Sr}/^{86}\text{Sr}$ ratios were measured in solution after dissolution and purification of Sr [Durango: 0.706321(5); Madagascar: 0.711814(5); Slyudyanka: 0.707705(4); Sumé: 0.707247(4); and Ipirá: 0.710487(4)]. The optimisation of both instrument setup and data reduction schemes was achieved through repeated measurements of calibration solutions and of apatite standards at four different rectangular-shaped laser ablation beam sizes (50 × 50, 25 × 25, 13 × 13 and 10 × 10 µm). Two complementary methods were developed for data reduction: *Method 1*, which corrects measured intensities for gas blank and instrumental mass bias only; and *Method 2*, which additionally corrects for isobaric interferences of $^{87}\text{Rb}^+$, ^{166}Lu , $^{168}\text{Er}^{++}$, ^{170}Y , ^{172}Y , ^{174}Y and $^{176}\text{Yb}^{++}$, $^{40}\text{Ca}^{44}\text{Ca}^+$, $^{40}\text{Ca}^{46}\text{Ca}^+$, $^{44}\text{Ca}^{43}\text{Ca}^+$ and $^{40}\text{Ca}^{48}\text{Ca}^+$. A precision of ca. 100 ppm (2 s.e.) can be achieved on the $^{87}\text{Sr}/^{86}\text{Sr}$ ratio with a 50 µm laser ablation beam when using *Method 2*, and it remains better than 3000 ppm at 10 µm with *Method 1*. *Method 1* gives precise and accurate $^{87}\text{Sr}/^{86}\text{Sr}$ ratios when $^{173}\text{Yb}^{++}$ is below the global limit of detection (with $\text{LOD}_{\text{global}} = 3$ s.d. of the means of all gas blanks measurements). When $^{173}\text{Yb}^{++}$ is above the $\text{LOD}_{\text{global}}$, *Method 2* should be preferred as it provides more accurate $^{87}\text{Sr}/^{86}\text{Sr}$ ratios. Overall, this study offers a robust and reliable approach for LA-MC-ICP-MS analysis of Sr isotopes in rock-forming apatite at a high spatial resolution (i.e. down to 10 µm), overcoming previous limitations associated with instrumental set up and data reduction.

Received 30th May 2023
 Accepted 29th August 2023

DOI: 10.1039/d3ja00177f
rsc.li/jaas

1. Introduction

Sr isotopes have applications in many fields of research, including Earth and planetary sciences,^{1,2} archaeology,^{3,4} palaeontology,^{5,6} environmental sciences,^{7–13} forensic sciences^{14,15} and agriculture.^{16–20} In Earth and planetary sciences, the Rb-Sr system is commonly used to constrain the age and the magmatic source of bulk rocks^{21–23} and Sr-rich minerals such as apatite,^{24–29} plagioclase,^{30–33} phlogopite,³⁴ or maskelynites from Martian meteorites.³⁵ If the geological material has not experienced secondary processes of metamorphism and/or alteration with time, the $^{87}\text{Sr}/^{86}\text{Sr}$ ratio can be used to constrain the petrogenesis of igneous rocks,^{36–40} to unravel magma sources in young volcanoes and magmatic

provinces,^{41–46} to date igneous rocks^{22,23} and to monitor the formation and the evolution of Earth's geochemical reservoirs through time.^{47–50}

Sr isotopes were initially analysed by thermal ionization mass spectrometry (TIMS), after separation and purification of Sr by ion exchange chromatography.^{51–53} In recent years, *in situ* analyses of Sr isotopes have advanced significantly, mirroring technical improvements in mass spectrometry. Both SIMS and LA-MC-ICP-MS techniques have been developed in parallel,^{29,54,55} and if one important challenge with SIMS is to find standards with Sr and rare earth elements (REE) concentrations matching those of the samples analysed, the major difficulty with LA-MC-ICP-MS is related to the presence of isobaric interferences from both atomic and polyatomic ions. As a consequence, Sr isotopes have remained challenging to analyse with a high level of precision and accuracy by LA-MC-ICP-MS. For instance, the interference of $^{87}\text{Rb}^+$ on $^{87}\text{Sr}^+$ induces a large uncertainty in the $^{87}\text{Sr}/^{86}\text{Sr}$ measured in samples with high Rb/Sr ratios, and accurate $^{87}\text{Sr}/^{86}\text{Sr}$ can hardly be obtained in samples with $\text{Rb/Sr} > 0.3$.^{28,56–61}

Géosciences Montpellier, CNRS & Université de Montpellier, Bât 22 CC60, Place Eugène Bataillon, 34095 Montpellier Cedex 5, France. E-mail: anda-ioana.buzenchi@umontpellier.fr

† Electronic supplementary information (ESI) available. See DOI: <https://doi.org/10.1039/d3ja00177f>



Amongst low Rb/Sr (<0.01) minerals, apatite ($(\text{Ca}_5\text{PO}_4)_3(\text{OH}, \text{Cl}, \text{F})$) has received increasing interest over the last two decades. This accessory phase is commonly found in magmatic rocks and sediments, it can be dated with the U-Th-Pb method,^{62–64} and its $^{87}\text{Sr}/^{86}\text{Sr}$ ratio remains unchanged since its crystallisation due to the negligible ingrowth of ^{87}Sr from the radioactive decay of ^{87}Rb . As a consequence, apatite has become a mineral of choice besides zircon in crustal evolution studies, although dissolution and recrystallisation under fluid circulation can drastically alter the $^{87}\text{Sr}/^{86}\text{Sr}$ ratio of apatites present in the rock matrix.^{65,66} To overcome this issue, recent studies have focused on measuring Sr isotopes in minute (*i.e.* 10–50 μm) apatite inclusions in more refractory and resistant minerals such as zircon.^{24,67–69}

Apatites have relatively high concentrations of calcium, phosphorus, erbium and ytterbium, which produce a number of isobaric interferences on $^{84}\text{Sr}^+$, $^{86}\text{Sr}^+$, $^{87}\text{Sr}^+$ and $^{88}\text{Sr}^+$.^{56,70} Previous studies have presented different protocols for doubly-charged REE interference corrections, and the most common approach is to monitor interference-free doubly-charged ions on half-masses (*e.g.*, $^{167}\text{Er}^{++}$ on m/z 83.5; $^{173}\text{Yb}^{++}$ on m/z 86.5) and to use natural isotopic abundances to calculate the contribution of interfering species.^{56,70} The isobaric interference of $^{40}\text{Ca}^{31}\text{P}^{16}\text{O}^+$ (or CaPO^+) on $^{87}\text{Sr}^+$ can be drastically reduced by controlling the instrumental conditions to reduce oxide production in the plasma,^{71,72} although this generally results in an overall decrease of sensitivity that affects analytical precision. Finally, although calcium dimers and argides interferences on Sr isotopes have been reported,^{26,73,74} their influence on the $^{87}\text{Sr}/^{86}\text{Sr}$ ratio remains debated and is often considered insignificant.^{56,57,61}

In this study we present a combination of new instrumental conditions and data reduction protocols for LA-MC-ICP-MS, and we apply this approach to the analysis of five apatite reference materials (Durango;⁷⁵ Madagascar;⁷⁶ Slyudyanka;⁶³ Sumé;⁷⁷ Ipirá), using laser ablation beam sizes between 50 \times 50 μm and 10 \times 10 μm . Both the precision and the accuracy of the $^{87}\text{Sr}/^{86}\text{Sr}$ ratio are improved compared to previous studies, which opens new perspectives for Sr isotope analyses at high spatial resolution.

2. Materials and methods

2.1. Rock-forming apatites used as reference material

Five apatites with a large range of Sr and REE contents were selected for this study. Madagascar, Durango, Slyudyanka and Sumé apatites were characterised in previous studies (Table 1), and Ipirá is a new in-house standard (C. Lana, *Pers. Comm.*). To ensure that the Sr isotope composition of the apatite fragments selected for LA-MC-ICP-MS analyses is consistent with the literature data, 40 to 100 mg of these fragments were dissolved in tri-distilled HNO_3 65% at 140 °C, and Sr was isolated in Teflon columns filled with Eichrom Sr-Spec ion-exchange resin following the approach of Pin *et al.*⁷⁸ Sr solutions were analysed with a Thermo Scientific MC-ICP-MS Neptune Plus at the AETE-ISO Platform (OSU-OREME, University of Montpellier), and the new Sr isotope data are summarised in Table 2.

2.1.1. Durango. Durango is a widely used reference material, which is sampled in an open pit iron mine near the Durango City in Mexico. It is a yellow-green fluorapatite, with a ID-TIMS U-Pb age of 32.716 ± 0.061 Ma.⁷⁵ It has the lowest Sr concentration (486 ppm) and the highest REE contents (Er = 34–83 ppm and Yb = 27–59 ppm) and (Er + Yb)/Sr ratio amongst apatites selected for this study (Table 1). The $^{87}\text{Sr}/^{86}\text{Sr}$ ratio of 0.706328 ± 0.000023 that Yang *et al.* obtained by TIMS and solution MC-ICP-MS was chosen as reference value.²⁹ Our new data for two fragments of Durango overlap within error (Table 2), with a mean $^{87}\text{Sr}/^{86}\text{Sr} = 0.706321 \pm 0.000005$ within error of the Yang *et al.* value.²⁹

2.1.2. Madagascar. Madagascar (or MAD) is a large fragment of apatite from the First Mine Discovery in Madagascar. Due to its homogenous U-Pb isotope composition, it has been widely used as a reference material for U-Pb dating, with a reference age of 474.25 ± 0.41 Ma.⁷⁶ It has a very high Sr concentration (1650 ppm), relatively high REE contents (Er = 21 ppm and Yb = 15 ppm), and its (Er + Yb)/Sr ratio is about 10 times greater than in Durango apatite (Table 1). The $^{87}\text{Sr}/^{86}\text{Sr}$ ratio of 0.711800 ± 0.000026 that Yang *et al.*²⁹ obtained by TIMS and solution MC-ICP-MS was chosen as reference value. The $^{87}\text{Sr}/^{86}\text{Sr}$ of 0.711814 ± 0.000005 that we obtained for one fragment of this apatite (Table 2) is within error of the Yang *et al.* value (Table 1).²⁹

2.1.3. Slyudyanka. Slyudyanka originates from the Slyudyanka complex, which is located on the southwest coast of Lake Baikal in Russia. It has a U-Pb age of 447.0 ± 7.3 Ma,⁶³ a high Sr concentration (1231 ppm), very low REE contents (Er = 5 ppm and Yb = 4 ppm) and the lowest (Er + Yb)/Sr ratio amongst apatites selected for this study (*i.e.* about 40 times lower than in Durango apatite; Table 1). The $^{87}\text{Sr}/^{86}\text{Sr}$ ratio of 0.707683 ± 0.000025 that Yang *et al.*²⁹ obtained by TIMS and solution MC-ICP-MS was chosen as reference. Our new data for two fragments of Slyudyanka overlap within error (Table 2), with a mean $^{87}\text{Sr}/^{86}\text{Sr} = 0.707706 \pm 0.000004$ within error of the Yang *et al.* value (Table 1).²⁹

2.1.4. Sumé. Sumé was recently proposed as a reference material by Lana *et al.*⁷⁷ It comes from the Borborema Province in NE Brazil and is found as large pockets of green-blueish apatite mineralisation within felsic gneisses of the Foresta Complex. It has a ID-TIMS U-Pb age of 568 ± 2 Ma,⁷⁷ a relatively high concentration of Sr (730–800 ppm) and REE (Yb = 20–23 ppm and Er = 13–15 ppm), and its (Er + Yb)/Sr ratio is about 4–5 times greater than in Durango apatite (Table 1). Lana *et al.* obtained an average $^{87}\text{Sr}/^{86}\text{Sr}$ isotope ratio of 0.7080 ± 0.0002 by LA-MC-ICP-MS, although they reported Sr isotope heterogeneities within different grains, with $^{87}\text{Sr}/^{86}\text{Sr}$ ranging between 0.70795 ± 0.00017 and 0.70850 ± 0.00026 .⁷⁷ Our new data for the two fragments of Sumé overlap within error (Table 2), with a mean $^{87}\text{Sr}/^{86}\text{Sr} = 0.707247 \pm 0.000004$ that is significantly lower than the mean value of Lana *et al.* (0.7080 ± 0.0002).⁷⁷

2.1.5. Ipirá. Ipirá is a colourless to green-blue apatite from the *ca.* 2 Ga Ipirá pegmatite in the State of Bahia in Brazil.⁸⁰ It frequently contains micrometric solid inclusions of unknown



Table 1 Summary of published data for the apatites used as reference material in this study

	Sr (ppm)	Er (ppm)	Yb (ppm)	Rb (ppm)	Er + Yb/Sr	$^{87}\text{Sr}/^{86}\text{Sr}$	2 s.d.	n	Method	Reference
Durango	486	34–83	27–59	0.13	0.12 to 0.28	0.706330	0.000030	3	TIMS ^a	Horstwood <i>et al.</i> ²⁶
						0.706340	0.000140	156	LA-MC-ICPMS	Yang <i>et al.</i> ²⁹
						0.706328	0.000023	13	TIMS + MC-ICPMS ^a	Yang <i>et al.</i> ²⁹
Madagascar	1650	21	15	0.25	0.021	0.706346	0.000516		LA-MC-ICPMS	Cao <i>et al.</i> ³⁰
						0.711800	0.000010	112	LA-MC-ICPMS	Yang <i>et al.</i> ²⁹
						0.711800	0.000002	11	TIMS + MC-ICPMS ^a	Yang <i>et al.</i> ²⁹
						0.712300	0.003000	6	CHILI	Boehnke <i>et al.</i> ⁶⁷
						0.712300	0.001800	43	SIMS	Gillespie <i>et al.</i> ²⁵
						0.711879	0.000157		LA-MC-ICPMS	Cao <i>et al.</i> ³⁰
Slyudyanka	1231	2	4	0.02	\sim 0.005	0.711900	0.000100	10	LA-MC-ICPMS	Huang <i>et al.</i> ⁷⁹
						0.707690	0.000015	110	LA-MC-ICPMS	Yang <i>et al.</i> ²⁹
						0.707680	0.000003	11	TIMS + MC-ICPMS ^a	Yang <i>et al.</i> ²⁹
Sumé	730–806	20–23	13–15	<0.1	\sim 0.045	0.708220	0.001690	28	SIMS	Gillespie <i>et al.</i> ²⁵
						0.708000	0.000200	14	LA-MC-ICPMS	Lana <i>et al.</i> ⁷⁷
Ipirá	256	17–7	12–6	<1.6	0.05 to 0.11	0.71049	0.00028	33	LA-MC-ICPMS	Cristiano Lana, <i>personal communication</i>

^a Analysis after chemical purification using conventional chromatographic column separation.

Table 2 Summary of solution MC-ICP-MS analyses of the five apatite standards selected for LA-MC-ICP-MS analyses

Sample name	$^{88}\text{Sr}(\text{v})$	$^{87}\text{Sr}/^{86}\text{Sr}$	2 s.e.
Durango_1	8.7	0.706319	0.000005
Durango_2	6.6	0.706322	0.000005
Madagascar	11.4	0.711814	0.000003
Slyudyanka_1	16.5	0.707705	0.000003
Slyudyanka_2	14.4	0.707706	0.000004
Sumé_1	10.5	0.707250	0.000003
Sumé_2	9.7	0.707245	0.000004
Ipirá	7.6	0.710487	0.000004

Table 3 Typical operating conditions for (LA)-MC-ICP-MS analyses

	Laser ablation	Solution
Neptune XT MC-ICP-MS		
RF power (W)	1350	1200
Focus voltage	−609	−611
Cool gas (L min ^{−1})	15	15
Auxiliary gas (L min ^{−1})	0.8	0.8
Sample gas (L min ^{−1})	1.026	1.100
Analyte Excite + with HelEx II 2-volumes ablation cell		
MFC1 He (L min ^{−1})	0.35	
MFC2 He (L min ^{−1})	0.17	
MFC3 N ₂ (mL min ^{−1})	10	
Repetition rate (Hz)	5	
Fluence (J cm ^{−2})	6	

composition, and to our knowledge no data have been published for this apatite. The $^{87}\text{Sr}/^{86}\text{Sr}$ of 0.710487 ± 0.000004 that we obtained for one fragment of Ipirá (Table 2) is consistent with preliminary LA-MC-ICP-MS data from the Universidade Federal de Ouro Preto in Brazil (C. Lana, *personal communication*).

2.2. Analytical conditions

Analyses were performed at the MILESTONE laboratory (Géosciences Montpellier), which is part of the ISOTOP-MTP platform of the RéGEF (<https://www.regef.fr/>). We used a Thermo Scientific Neptune XT multicollector inductively coupled plasma mass spectrometer (MC-ICP-MS), for which the sensitivity was improved by using an Edwards nXL110i dry interface pump in combination with a Jet sample cone and a X skimmer cone. Typical operating conditions are outlined in Table 3 and the Faraday cup configuration is detailed in Table 4.

For *in situ* analyses, the MC-ICP-MS was coupled to a Tele-dyne Cetac Analyte Excite + excimer laser, which includes an optional 'X-Y Theta' dynamic aperture that allows rectangular-shaped laser beams of any aspect ratio and orientation to be generated. Tuning for optimal sensitivity, signal stability and best peak shape were performed daily in rastering ablation mode on the Durango apatite, with a $50 \times 50 \mu\text{m}$ laser ablation beam, a scan speed of $5 \mu\text{m s}^{-1}$, a fluence of 6 J cm^{-2} and a repetition rate of 6 Hz. Oxide production in the plasma was monitored with the UO^+/U^+ ratio, and optimal plasma conditions ($\text{UO}^+/\text{U}^+ < 0.1\%$) were achieved by tuning the torch position and the Ar, He and N₂ gas flow rates. Apatite analyses were done at four different laser ablation beam sizes: $50 \times 50 \mu\text{m}$, $25 \times 25 \mu\text{m}$, $13 \times 13 \mu\text{m}$ and $10 \times 10 \mu\text{m}$. The integration time of the Neptune was set at 1 s per cycle. A gas line wash-out of 40 cycles and an on-peak gas blank of 120 cycles were analysed before each apatite measurement of 60 cycles.

The way particles are transported from the ablation cell towards the plasma is key to achieve high-precision measurements by LA-MC-ICP-MS.^{81,82} Several configurations have been tested, including the smoothing "SQUID" manifold that splits the mixture of gas and sample aerosol flow into ten nylon tubes of differing lengths, such that after recombination into one gas line a smooth signal is produced;⁸¹ and the Aerosol Rapid Introduction System (ARIS) that consists of a 1 m long polyether



Table 4 Neptune cup configuration for Sr isotope analyses, and potential isobaric interferences for each mass

Faraday cup Amplifier (ohm)	L4 10^{11}	L3 10^{11}	L2 10^{11}	L1 10^{11}	C 10^{11}	H1 10^{11}	H2 10^{11}	H3 10^{11}	H4 10^{11}
<i>m/z</i>	83	83.5	84 $^{84}\text{Sr}^+$	85	85.5	86 $^{86}\text{Sr}^+$	86.5	87 $^{87}\text{Sr}^+$	88 $^{88}\text{Sr}^+$
Sr									
Rb				$^{85}\text{Rb}^+$				$^{87}\text{Rb}^+$	
Kr	$^{83}\text{Kr}^+$		$^{84}\text{Kr}^+$			$^{86}\text{Kr}^+$			
Er	$^{166}\text{Er}^{++}$	$^{167}\text{Er}^{++}$	$^{168}\text{Er}^{++}$	$^{170}\text{Er}^{++}$					
Yb			$^{168}\text{Yb}^{++}$	$^{170}\text{Yb}^{++}$	$^{171}\text{Yb}^{++}$	$^{172}\text{Yb}^{++}$	$^{173}\text{Yb}^{++}$	$^{174}\text{Yb}^{++}$	$^{176}\text{Yb}^{++}$
Lu									$^{176}\text{Lu}^{++}$
Hf									$^{176}\text{Hf}^{++}$
Ca dimers	$^{40}\text{Ca}^{43}\text{Ca}^+$		$^{42}\text{Ca}^{42}\text{Ca}^+$ $^{40}\text{Ca}^{44}\text{Ca}^+$			$^{42}\text{Ca}^{44}\text{Ca}^+$ $^{40}\text{Ca}^{46}\text{Ca}^+$ $^{43}\text{Ca}^{43}\text{Ca}^+$		$^{43}\text{Ca}^{44}\text{Ca}^+$	$^{40}\text{Ca}^{48}\text{Ca}^+$ $^{44}\text{Ca}^{44}\text{Ca}^+$ $^{42}\text{Ca}^{46}\text{Ca}^+$ $^{48}\text{Ca}^{40}\text{Ar}^+$
Ca argides		$^{43}\text{Ca}^{40}\text{Ar}^+$		$^{44}\text{Ca}^{40}\text{Ar}^+$ $^{46}\text{Ca}^{38}\text{Ar}^+$ $^{48}\text{Ca}^{36}\text{Ar}^+$			$^{46}\text{Ca}^{40}\text{Ar}^+$ $^{48}\text{Ca}^{38}\text{Ar}^+$		

ether-ketone (PEEK) capillary tubing that penetrates the injector with a specific adapter to the torch. The ARIS allows a more efficient transfer of the particles from the ablation site to the torch, while also decreasing oxide formation.⁸² For Sr isotopes, a 2–3 times improvement of both the instrumental sensitivity and the internal precision of the measurements was observed with the ARIS (ESI Fig. 1†), which is why this system was selected for this study.

For solution analyses, solutions were sprayed to the instrument's torch *via* a 100 $\mu\text{L min}^{-1}$ nebuliser and a cyclonic spray chamber. The instrumental sensitivity was 0.3 V ppb⁻¹ for Sr

isotopes, and 40 cycles of 1 s each were integrated for each measurement.

The MC-ICP-MS cup configuration that is commonly used to measure Sr isotopes involves the alignment of the cups measuring interference-free doubly-charged Er⁺⁺ and Yb⁺⁺ ions (*i.e.* $m/z = 83.5$ for $^{167}\text{Er}^{++}$, 85.5 for $^{171}\text{Yb}^{++}$ and 86.5 for $^{173}\text{Yb}^{++}$) with the other cups measuring Sr and Rb isotopes. The on-peak measurements of $^{171}\text{Yb}^{++}$, $^{173}\text{Yb}^{++}$ and $^{167}\text{Er}^{++}$, and the natural ratios between these isotopes and the Yb⁺⁺ and Er⁺⁺ ions interfering on m/z 84, 85, 86, 87 and 88, are commonly used to calculate the intensities of interference-free Rb and Sr

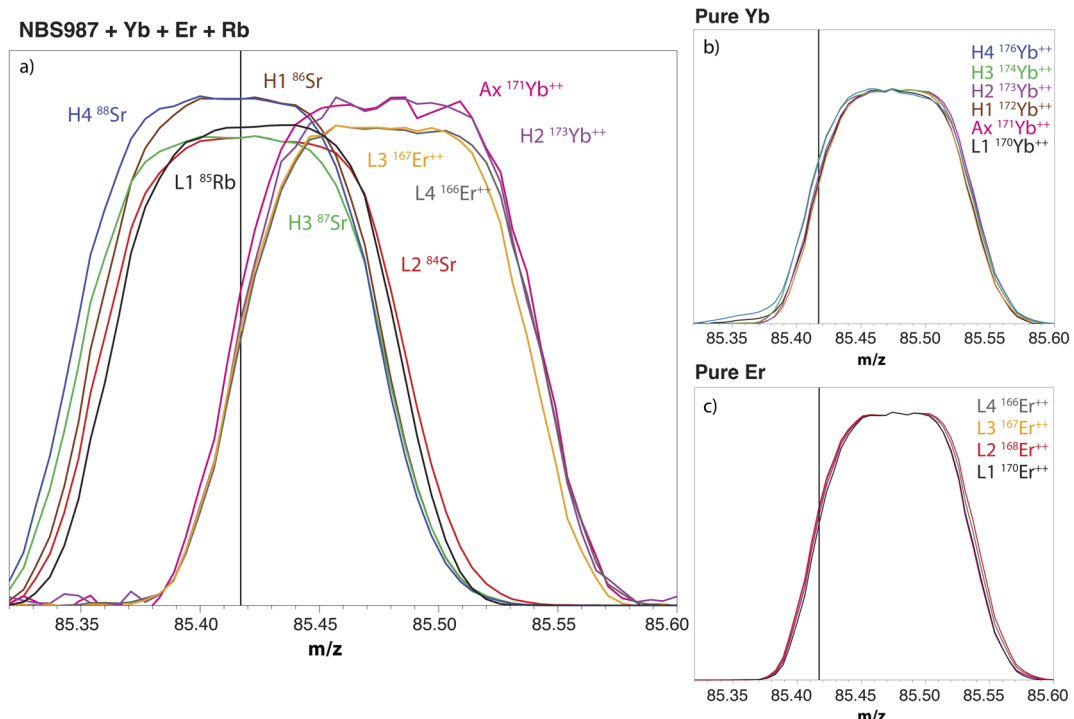


Fig. 1 Mass scans of (a) a solution of 100 ppb NIST SRM 987 doped with 20 ppb Yb, 20 ppb Er and 5 ppb Rb; (b) a solution of pure Yb; and (c) a solution of pure Er. Factors were applied to the intensities measured in order to obtain peaks with similar heights. The vertical line indicates the m/z set for the central cup.



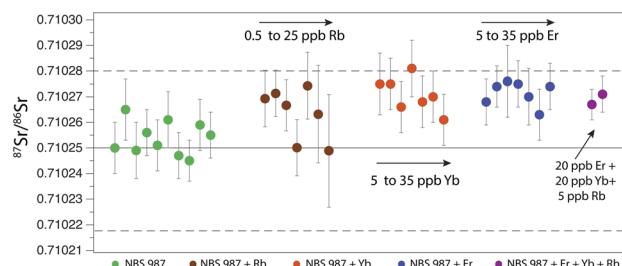


Fig. 2 Interferences and mass bias corrected $^{87}\text{Sr}/^{86}\text{Sr}$ ratios in solutions containing pure NIST SRM 987 spiked with various concentrations of interfering species (Rb, Yb and Er). Error bars are 2 s.e. Horizontal solid and dashed lines represent the average value and the 2 s.d., respectively, of 1279 TIMS analyses of NIST SRM 987 reference material (downloaded from <https://georem.mpch-mainz.gwdg.de/>).

isotopes.^{56,70} However, and as a major limitation of this approach, doubly-charged Er and Yb ions have a peak high that is shifted by *ca.* 0.05–0.07 amu from the peak highs of the Rb and Sr ions on which they interfere (Fig. 1).^{56,70} As a result, the on-peak measurement of $^{171}\text{Yb}^{++}$, $^{173}\text{Yb}^{++}$ and $^{167}\text{Er}^{++}$ leads to an overestimation of the intensities of the interfering Yb^{++} and Er^{++} ions on the cups measuring Rb and Sr isotopes. To avoid this issue, we used a new approach in which the interference-free doubly-charged $^{171}\text{Yb}^{++}$, $^{173}\text{Yb}^{++}$ and $^{168}\text{Er}^{++}$ were aligned with the Yb^{++} and Er^{++} ions interfering on m/z 84, 85, 86, 87 and 88 (Fig. 1).

2.3. Interferences and mass bias correction

The raw data intensities were reduced offline using an in-house Excel spreadsheet. For each m/z of interest, the mean intensities of the gas blank were calculated after applying a 2 s.d. threshold for outlier rejection, and the gas blank was subtracted from the raw intensities measured in the sample. We assumed that krypton is only present in the gas and that the contribution of Kr on m/z 83, 84 and 86 is negligible after gas blank correction. Our approach for the correction of

interferences on m/z 84, 85, 86, 87 and 88 includes three successive steps, after which a fourth step of mass bias correction was applied.

2.3.1. Step 1: Doubly-charged Er and Yb correction. Interferences produced by doubly-charged Er and Yb ions can significantly alter the measurement of Sr isotopes by LA-MC-ICP-MS. $^{166}\text{Er}^{++}$, $^{168}\text{Er}^{++}$ and $^{170}\text{Er}^{++}$ interfere on masses 83, 84 and 85, respectively, while $^{170}\text{Yb}^{++}$, $^{172}\text{Yb}^{++}$, $^{174}\text{Yb}^{++}$ and $^{176}\text{Yb}^{++}$ interfere on masses 85, 86, 87 and 88, respectively^{56,61,70} (Table 2).

For ytterbium, the interference-free doubly-charged $^{173}\text{Yb}^{++}$ was measured on m/z 86.5. The ratios used to calculate the amount of doubly-charged Yb ions interfering on each mass of interest were defined from the analysis of pure Yb solutions, with $^{168}\text{Yb}/^{173}\text{Yb} = 0.007651$; $^{170}\text{Yb}/^{173}\text{Yb} = 0.185183$; $^{172}\text{Yb}/^{173}\text{Yb} = 1.163427$; $^{174}\text{Yb}/^{173}\text{Yb} = 2.250953$; and $^{176}\text{Yb}/^{173}\text{Yb} = 0.795370$. Yb-free intensities were calculated from eqn (1)–(5), in which the subscripts *m* and *IC* are for *measured* and *interference-corrected* intensities, respectively:

$$^{84}\text{Sr}_{\text{YbIC}}^+ = ^{84}\text{Sr}_m^+ - ^{168}\text{Yb}/^{173}\text{Yb}_{(0.007651)} \times ^{173}\text{Yb}_m^{++} \quad (1)$$

$$^{85}\text{Rb}_{\text{YbIC}}^+ = ^{85}\text{Rb}_m^+ - ^{170}\text{Yb}/^{173}\text{Yb}_{(0.185183)} \times ^{173}\text{Yb}_m^{++} \quad (2)$$

$$^{86}\text{Sr}_{\text{YbIC}}^+ = ^{86}\text{Sr}_m^+ - ^{172}\text{Yb}/^{173}\text{Yb}_{(1.163427)} \times ^{173}\text{Yb}_m^{++} \quad (3)$$

$$^{87}\text{Sr}_{\text{YbIC}}^+ = ^{87}\text{Sr}_m^+ - ^{174}\text{Yb}/^{173}\text{Yb}_{(2.250953)} \times ^{173}\text{Yb}_m^{++} \quad (4)$$

$$^{88}\text{Sr}_{\text{YbIC}}^+ = ^{88}\text{Sr}_m^+ - ^{176}\text{Yb}/^{173}\text{Yb}_{(0.795370)} \times ^{173}\text{Yb}_m^{++} \quad (5)$$

For erbium, the interference-free doubly-charged $^{167}\text{Er}^{++}$ was measured on m/z 83.5. The ratios used to calculate the amount of doubly-charged Er ions interfering on each mass of interest were defined from the analysis of pure Er solutions, with $^{170}\text{Er}/^{167}\text{Er} = 0.640024$; $^{168}\text{Er}/^{167}\text{Er} = 1.275114$; and $^{166}\text{Er}/^{167}\text{Er} = 1.536252$. Er-free intensities were calculated from eqn (6)–(8), in which the subscripts *m* and *IC* are for *measured* and *interference-corrected* intensities, respectively:

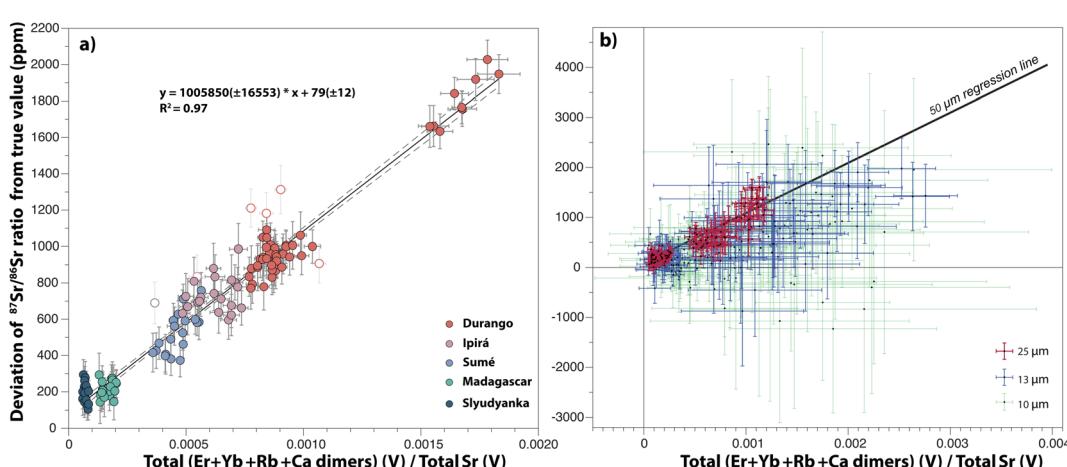


Fig. 3 Accuracy of the mass bias corrected $^{87}\text{Sr}/^{86}\text{Sr}$ ratio (expressed as the deviation in ppm from the reference value) as a function of the contribution of interfering species on measured Sr intensities. (a) Apatite analyses with a 50 μm laser ablation beam size. Empty symbols were not used for the regression. (b) Apatite analyses at 25 μm , 13 μm and 10 μm .

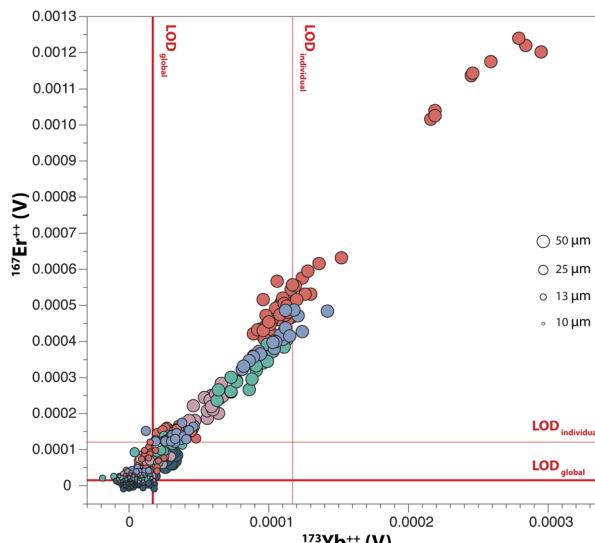


Fig. 4 Variation of $^{167}\text{Er}^{++}$ and $^{173}\text{Yb}^{++}$ intensities measured in apatite standards, for laser ablation beam sizes ranging between 50 μm and 10 μm . Colour codes are same as in Fig. 3a. The $\text{LOD}_{\text{individual}}$ (thin red lines) is the average 3 s.d. of individual gas blank intensities, and the $\text{LOD}_{\text{global}}$ (thick red lines) is the 3 s.d. of 460 gas blank analyses.

$$^{40}\text{Ca}^{43}\text{Ca}_{\text{ErIC}}^+ = ^{40}\text{Ca}^{43}\text{Ca}_m^+ - ^{166}\text{Er} / ^{167}\text{Er}_{(1.536252)} \times ^{167}\text{Er}_m^{++} \quad (6)$$

$$^{84}\text{Sr}_{\text{ErIC}}^+ = ^{84}\text{Sr}_{\text{YbIC}}^+ - ^{168}\text{Er} / ^{167}\text{Er}_{(1.275114)} \times ^{167}\text{Er}_m^{++} \quad (7)$$

$$^{85}\text{Rb}_{\text{ErIC}}^+ = ^{85}\text{Rb}_{\text{YbIC}}^+ - ^{170}\text{Er} / ^{167}\text{Er}_{(0.640024)} \times ^{167}\text{Er}_m^{++} \quad (8)$$

2.3.2. Step 2: Ca dimers correction. We assumed that the remaining intensity on m/z 83 after subtracting $^{83}\text{Kr}^+$ and $^{166}\text{Er}^{++}$ is entirely due to the interference of $^{40}\text{Ca}^{43}\text{Ca}^+$. The ratios used to calculate the amount of Ca dimers interfering on each mass of interest were the natural ratios published by Rosman and Taylor ($^{40}\text{Ca}^{44}\text{Ca} / ^{40}\text{Ca}^{43}\text{Ca} = 15.451850$; $^{40}\text{Ca}^{46}\text{Ca} / ^{40}\text{Ca}^{43}\text{Ca} = 0.029630$; $^{44}\text{Ca}^{43}\text{Ca} / ^{40}\text{Ca}^{43}\text{Ca} = 0.021518$; $^{40}\text{Ca}^{48}\text{Ca} / ^{40}\text{Ca}^{43}\text{Ca} = 1.385185$).⁸³ Ca dimers-free intensities were calculated from eqn (9)–(12), in which the subscripts *IC* are for *interference-corrected* intensities:

$$^{84}\text{Sr}_{\text{CaIC}}^+ = ^{84}\text{Sr}_{\text{ErIC}}^+ - ^{40}\text{Ca}^{44}\text{Ca} / ^{40}\text{Ca}^{43}\text{Ca}_{(15.451850)} \times ^{40}\text{Ca}^{43}\text{Ca}_{\text{ErIC}}^+ \quad (9)$$

$$^{86}\text{Sr}_{\text{CaIC}}^+ = ^{86}\text{Sr}_{\text{ErIC}}^+ - ^{40}\text{Ca}^{46}\text{Ca} / ^{40}\text{Ca}^{43}\text{Ca}_{(0.029630)} \times ^{40}\text{Ca}^{43}\text{Ca}_{\text{ErIC}}^+ \quad (10)$$

$$^{87}\text{Sr}_{\text{CaIC}}^+ = ^{87}\text{Sr}_{\text{ErIC}}^+ - ^{44}\text{Ca}^{43}\text{Ca} / ^{40}\text{Ca}^{43}\text{Ca}_{(0.021518)} \times ^{40}\text{Ca}^{43}\text{Ca}_{\text{ErIC}}^+ \quad (11)$$

$$^{88}\text{Sr}_{\text{CaIC}}^+ = ^{88}\text{Sr}_{\text{ErIC}}^+ - ^{40}\text{Ca}^{48}\text{Ca} / ^{40}\text{Ca}^{43}\text{Ca}_{(1.385185)} \times ^{40}\text{Ca}^{43}\text{Ca}_{\text{ErIC}}^+ \quad (12)$$

We note however that the Ca dimers correction produces insignificant changes in the calculation of the $^{87}\text{Sr} / ^{86}\text{Sr}$ ratio at the level of precision achieved in our study. This is consistent with the previous observations of Ramos *et al.*, Yang *et al.*, and Irrgeher *et al.*^{56,57,70}

2.3.3. Step 3: Rb correction. The interference-free $^{85}\text{Rb}^+$ was measured on m/z 85, and the ratio used to calculate the amount of $^{87}\text{Rb}^+$ interfering on $^{87}\text{Sr}^+$ was defined from repeated measurements of NIST SRM 987 solutions spiked with pure Rb solutions ($^{87}\text{Rb} / ^{85}\text{Rb} = 2.589745$), following the approach described by Horstwood *et al.*²⁶ Since only one rubidium isotope is interference-free (*i.e.* $^{85}\text{Rb}^+$; Table 4), the mass bias of Rb (βRb) could not be calculated during apatite analyses and βSr was used instead of βRb , assuming that instrumental mass bias discrimination is reasonably similar for Rb and Sr.^{26,27} Rb-free intensities were calculated from eqn (13), in which the subscripts *m* and *IC* are for *measured* and *interference-corrected* intensities, respectively:

$$^{87}\text{Sr}_{\text{RbIC}}^+ = ^{87}\text{Sr}_{\text{CaIC}}^+ - ^{85}\text{Rb}_{\text{ErIC}}^+ \times ^{87}\text{Rb} / ^{85}\text{Rb}_{(2.589745)} / e^{(\beta\text{Sr} \times \ln(M87 / M85))} \quad (13)$$

with:

$$\beta\text{Sr} = \ln(^{88}\text{Sr} / ^{86}\text{Sr}_{\text{natural}}) / \ln(M88 / M86)$$

2.3.4. Step 4: Mass bias correction. Finally, an exponential mass bias correction was applied to calculate the final $^{87}\text{Sr} / ^{86}\text{Sr}$ ratio, following eqn (14):

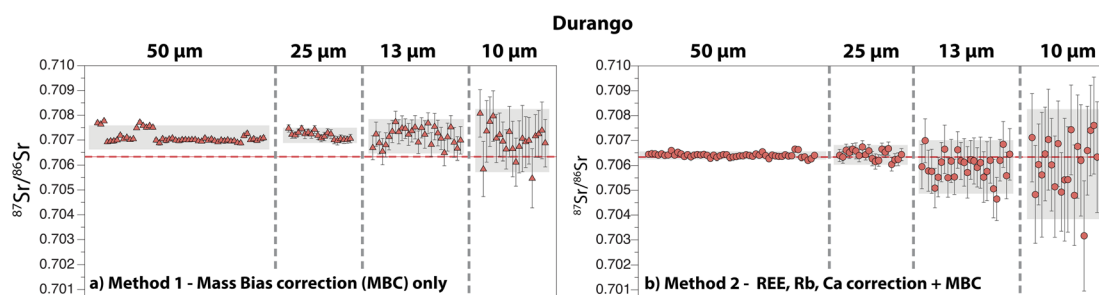


Fig. 5 Compilation of $^{87}\text{Sr} / ^{86}\text{Sr}$ ratios obtained by LA-ICP-MS on the Durango apatite, with laser ablation beam sizes ranging between 50 μm and 10 μm . (a) *Method 1* and (b) *Method 2* for data reduction (see text for details). Error bars are 2 s.e., with a number of symbols larger than error bars. Grey fields represent the 2 s.d. of repeated measurements at a given laser ablation beam size. Solid and dashed red lines are the published mean reference value and associated 2 s.d., respectively, for the Durango apatite.²⁹



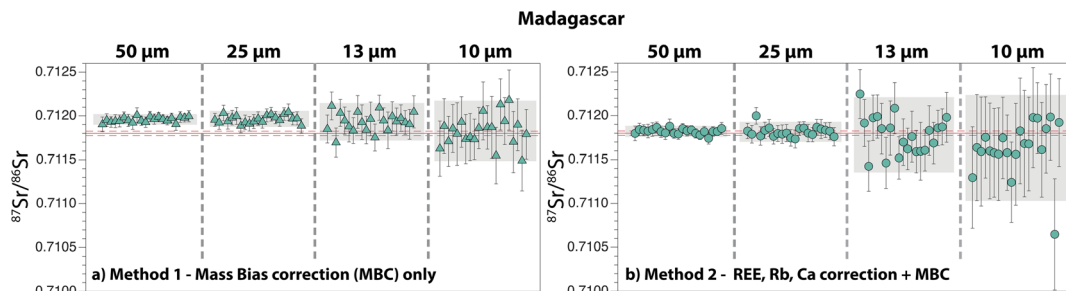


Fig. 6 Compilation of $^{87}\text{Sr}/^{86}\text{Sr}$ ratios obtained by LA-ICP-MS on the Madagascar apatite, with laser ablation beam sizes ranging between 50 μm and 10 μm . (a) *Method 1* and (b) *Method 2* for data reduction. See caption of Fig. 5 for details. Solid and dashed red lines are the published mean reference value and associated 2 s.d., respectively, for the Madagascar apatite.²⁹

$$^{87}\text{Sr}/^{86}\text{Sr}_{\text{mbc}} = ^{87}\text{Sr}_{\text{RbIC}}^{+}/^{86}\text{Sr}_{\text{CaIC}}^{+} \times (\text{M87}/\text{M86})^{\text{BSr}} \quad (14)$$

where $^{87}\text{Sr}/^{86}\text{Sr}_{\text{mbc}}$ is the final mass bias-corrected ratio, and $(\text{M87}/\text{M86})^{\text{BSr}}$ is the mass bias correction factor.

2.4. Validation of the approach used for data reduction

A summary of solution analyses of a pure Sr standard (NIST SRM 987), and of NIST SRM 987 spiked with various amounts of pure solutions of Rb, Er and Yb, is given in Fig. 2 and ESI Table 1.[†] For solutions containing interfering elements, analyses were separated into 5 groups of solutions that contain NIST SRM 987 as well as (1) Rb; (2) Yb; (3) Er; (4) Yb + Er; and (5) Rb + Yb + Er. When using the approach described in Section 2.3 for interferences and mass bias correction, all $^{87}\text{Sr}/^{86}\text{Sr}$ ratios plot within error of the reference value of Thirlwall (*i.e.* $^{87}\text{Sr}/^{86}\text{Sr} = 0.710248 \pm 0.000024$; 2 s.d.), and within error of high-precision TIMS values published for NIST SRM 987 in the past 20 years (0.710249 ± 0.000031). Overall, these results further validate our approach.

3. LA-MC-ICP-MS analyses

3.1. Impact of interferences on the $^{87}\text{Sr}/^{86}\text{Sr}$ ratio

A summary of 457 analyses performed on Durango, Madagascar, Slyudyanka, Sumé and Ipirá apatites at four laser ablation beam sizes (50 μm , 25 μm , 13 μm and 10 μm) is presented in ESI Table 2.[†] The deviation in ppm of the $^{87}\text{Sr}/^{86}\text{Sr}$ corrected only from mass bias, from the reference $^{87}\text{Sr}/^{86}\text{Sr}$ ratio of each apatite standard, is

plotted as a function of the ratio of the sum of intensities of interfering species over the total Sr intensity in Fig. 3. A positive correlation is observed, and this correlation becomes more evident for analyses performed with the largest laser ablation beam size (*i.e.* 50 μm ; Fig. 3a), as higher intensities are measured on Faraday cups. For smaller beam sizes, especially at 10 μm , the lower intensities measured on Faraday cups drastically alter the precision, and the need for correcting small interferences becomes less evident. This is particularly true for apatites with the lowest ratios of interfering species over total Sr (Fig. 3b).

$^{167}\text{Er}^{++}$ intensities measured on m/z 83.5 are plotted against $^{173}\text{Yb}^{++}$ intensities measured on m/z 86.5 in Fig. 4. A positive correlation is observed, which is consistent with the similar behaviour of heavy REE in rock-forming apatites during crystallisation. The need for interferences correction is highly dependent on the extent to which small intensities can be detected. Accordingly, the limit of detection for intensities measured on m/z 83.5 and 86.5 was calculated in two different ways in Fig. 4: (i) as the 3 s.d. of individual gas blank measurements before each apatite analysis ($\text{LOD}_{\text{individual}}$); and (ii) as the 3 s.d. of the mean values of all gas blanks ($\text{LOD}_{\text{global}}$). The $\text{LOD}_{\text{global}}$ and $\text{LOD}_{\text{individual}}$ are taken here as the lower and upper bounds, respectively, of the threshold from which intensities measured on Faraday cups should be used for interferences correction. Based on this observation and the correlation evidenced in Fig. 3, we explored two different methods for data reduction of the five apatite standards:

- *Method 1*, in which the blank-corrected $^{87}\text{Sr}/^{86}\text{Sr}$ ratio is only corrected from the mass bias.

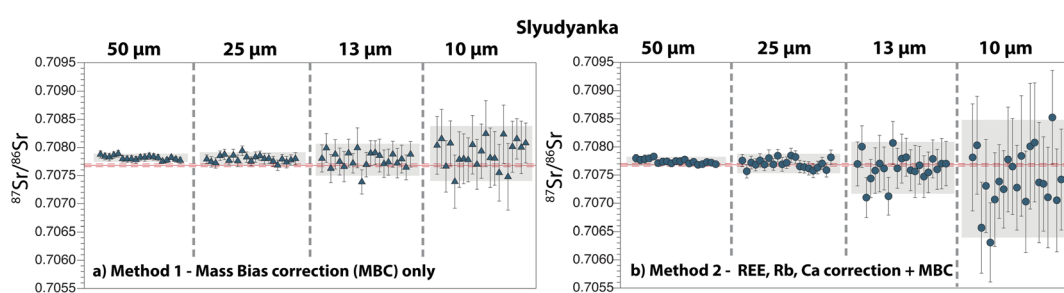


Fig. 7 Compilation of $^{87}\text{Sr}/^{86}\text{Sr}$ ratios obtained by LA-ICP-MS on the Slyudyanka apatite, with laser ablation beam sizes ranging between 50 μm and 10 μm . (a) *Method 1* and (b) *Method 2* for data reduction. See caption of Fig. 5 for details. Solid and dashed red lines are the published mean reference value and associated 2 s.d., respectively, for the Slyudyanka apatite.²⁹



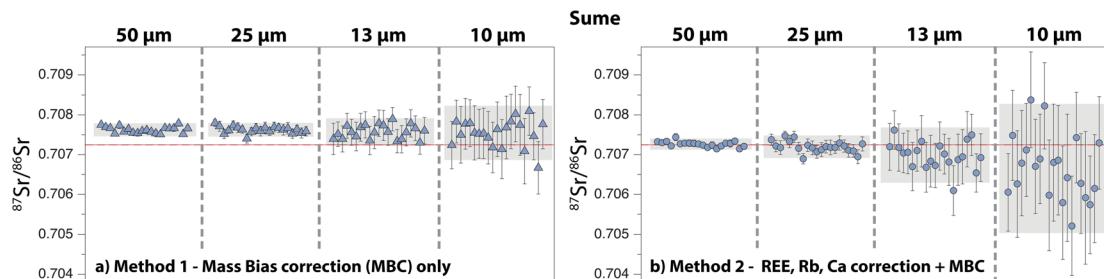


Fig. 8 Compilation of $^{87}\text{Sr}/^{86}\text{Sr}$ ratios obtained by LA-ICP-MS on the Sumé apatite, with laser ablation beam sizes ranging between 50 μm and 10 μm . (a) Method 1 and (b) Method 2 for data reduction. See caption of Fig. 5 for details. The solid red line is the solution MC-ICP-MS value obtained in this study.

• Method 2, in which the blank-corrected $^{87}\text{Sr}/^{86}\text{Sr}$ ratio is corrected from both interferences and mass bias, following the approach detailed in Section 2.3.

3.2. Durango

A summary of 121 Durango apatite analyses is presented in Fig. 5. The internal precision of individual measurements, which is given by the 2 s.e. of the mean of the number of cycles integrated, varies as a function of the laser ablation beam size and the method used. The 2 s.e. of the $^{87}\text{Sr}/^{86}\text{Sr}$ ratio ranges between 150 ppm (50 μm) and 1880 ppm (10 μm) for Method 1, and between 160 ppm (50 μm) and 3550 ppm (10 μm) for Method 2. Repeated measurements with Method 2 give average $^{87}\text{Sr}/^{86}\text{Sr}$ ratios that are all within error of both the reference value and our new solution value (50 μm : 0.706392 ± 0.000163 ; 25 μm : 0.706421 ± 0.000391 ; 13 μm : 0.705935 ± 0.001069 ; 10 μm : 0.706047 ± 0.002208 ; 2 s.d.) (Tables 1 and 2; ESI Table 2†). When Method 1 is used, a shift towards higher $^{87}\text{Sr}/^{86}\text{Sr}$ is observed, and only the average data at 10 μm are within error of the reference value (50 μm : 0.707106 ± 0.000484 ; 25 μm : 0.707190 ± 0.000305 ; 13 μm : 0.707153 ± 0.000692 ; 10 μm : 0.706985 ± 0.001266).

3.3. Madagascar

Eighty-four analyses Madagascar apatite analyses are summarised in Fig. 6. The 2 s.e. of the $^{87}\text{Sr}/^{86}\text{Sr}$ ratio ranges between 120 ppm (50 μm) and 500 ppm (10 μm) for Method 1, and

between 120 ppm (50 μm) and 890 ppm (10 μm) for Method 2. Repeated measurements with Method 2 give average $^{87}\text{Sr}/^{86}\text{Sr}$ ratios that are all within error of both the reference value and our new solution value (50 μm : 0.711821 ± 0.000063 ; 25 μm : 0.711816 ± 0.000115 ; 13 μm : 0.711783 ± 0.000429 ; 10 μm : 0.711633 ± 0.000603 ; 2 s.d.) (Tables 1 and 2; ESI Table 2†). When Method 1 is used, a shift towards higher $^{87}\text{Sr}/^{86}\text{Sr}$ is observed at 50 μm and 25 μm , whereas the average data at 13 μm and 10 μm are within error of the reference value (50 μm : 0.711957 ± 0.000060 ; 25 μm : 0.711963 ± 0.000092 ; 13 μm : 0.711930 ± 0.000214 ; 10 μm : 0.711827 ± 0.000344).

3.4. Slyudyanka

Fig. 7 shows a summary of 85 Slyudyanka apatite analyses. The 2 s.e. of the $^{87}\text{Sr}/^{86}\text{Sr}$ ratio ranges between 100 ppm (50 μm) and 840 ppm (10 μm) for Method 1, and between 100 ppm (50 μm) and 1570 ppm (10 μm) for Method 2. Repeated measurements with Method 2 give average $^{87}\text{Sr}/^{86}\text{Sr}$ ratios that are all within error of both the reference value and our new solution value (50 μm : 0.707743 ± 0.000082 ; 25 μm : 0.707706 ± 0.000173 ; 13 μm : 0.707629 ± 0.000460 ; 10 μm : 0.707439 ± 0.001042 ; 2 s.d.) (Tables 1 and 2; ESI Table 2†). When Method 1 is used, a shift towards higher $^{87}\text{Sr}/^{86}\text{Sr}$ is observed at 50 μm and 25 μm , whereas the average data at 13 μm and 10 μm are within error of the reference value (50 μm : 0.707817 ± 0.000073 ; 25 μm : 0.707797 ± 0.000118 ; 13 μm : 0.707782 ± 0.000284 ; 10 μm : 0.707893 ± 0.000488).

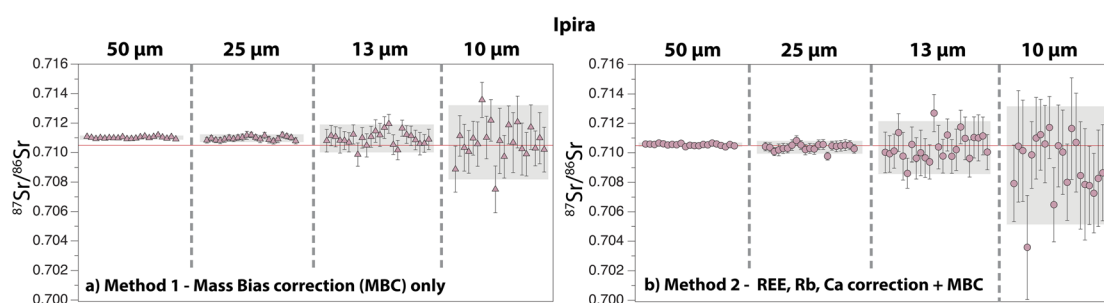


Fig. 9 Compilation of $^{87}\text{Sr}/^{86}\text{Sr}$ ratios obtained by LA-ICP-MS on the Ipirá apatite, with laser ablation beam sizes ranging between 50 μm and 10 μm . (a) Method 1 and (b) Method 2 for data reduction. See caption of Fig. 5 for details. The solid red line is the solution MC-ICP-MS value obtained in this study.



3.5. Sumé

A summary of 83 Sumé apatite analyses is shown in Fig. 8. The 2 s.e. of the $^{87}\text{Sr}/^{86}\text{Sr}$ ratio ranges between 115 ppm (50 μm) and 1160 ppm (10 μm) for *Method 1*, and between 125 ppm (50 μm) and 2360 ppm (10 μm) for *Method 2*. Repeated measurements with *Method 2* give average $^{87}\text{Sr}/^{86}\text{Sr}$ ratios that are all within error of our new solution value but lower than the value of 0.7080 ± 0.0002 published by Lana *et al.*⁷⁷ (50 μm : 0.707266 ± 0.000139 ; 25 μm : 0.707199 ± 0.000253 ; 13 μm : 0.706987 ± 0.000636 ; 10 μm : 0.706634 ± 0.001743 ; 2 s.d.) (Tables 1 and 2; ESI Table 2†). When *Method 1* is used, a shift towards higher $^{87}\text{Sr}/^{86}\text{Sr}$ is observed at 50 μm and 25 μm , whereas the average data at 13 μm and 10 μm are within error of the reference value (50 μm : 0.707624 ± 0.000163 ; 25 μm : 0.707394 ± 0.000170 ; 13 μm : 0.707274 ± 0.000422 ; 10 μm : 0.707303 ± 0.000752).

3.6. Ipirá

Eighty-seven analyses were performed on this apatite standard, and the results are summarised in Fig. 9. The 2 s.e. of the $^{87}\text{Sr}/^{86}\text{Sr}$ ratio ranges between 155 ppm (50 μm) and 3115 ppm (10 μm) for *Method 1*, and between 190 ppm (50 μm) and 5340 ppm (10 μm) for *Method 2*. Repeated measurements with *Method 2* give average $^{87}\text{Sr}/^{86}\text{Sr}$ ratios that are all within error of our new solution value (50 μm : 0.710542 ± 0.000147 ; 25 μm : 0.710370 ± 0.000435 ; 13 μm : 0.710359 ± 0.001786 ; 10 μm : 0.709147 ± 0.004009 ; 2 s.d.) (Tables 1 and 2; ESI Table 2†). When *Method 1* is used, a shift towards higher $^{87}\text{Sr}/^{86}\text{Sr}$ is observed at 50 μm and 25 μm , whereas average data at 13 μm and 10 μm are within error of the reference value (50 μm : 0.711012 ± 0.000139 ; 25 μm : 0.710973 ± 0.000262 ; 13 μm : 0.710958 ± 0.000949 ; 10 μm : 0.710704 ± 0.002513).

3.7. Summary

Our new LA-MC-ICP-MS data for the Durango, Madagascar and Slyudyanka apatites are in good agreement with both our new solution values and published values for these standards (Fig. 5, 6 and 7; Tables 1 and 2). For Sumé, the $^{87}\text{Sr}/^{86}\text{Sr}$ obtained with both *Method 1* and *Method 2* are clearly lower than the value published by Lana *et al.*⁷⁷ Importantly, these authors have noted that the Sumé apatite may not have a homogeneous $^{87}\text{Sr}/^{86}\text{Sr}$ depending on which sample batches are analysed. This is confirmed by our data, and the good agreement between our solution and laser ablation data for fragments issued from the same sample batch validates the robustness of our analytical approach. However, the presence of small Sr isotope heterogeneities in the five apatites analysed should not be ruled out at the micrometre scale, since a few individual analyses at 13 μm and 10 μm do not overlap reference values (Fig. 5, 6, 7, 8 and 9). Overall, the Durango, Madagascar, Slyudyanka, Sumé and Ipirá apatites, which have a large range of Sr and REE compositions as well as homogeneous Sr isotope ratios at the scale of the fragments analysed, constitute excellent reference materials for LA-MC-ICP-MS studies.

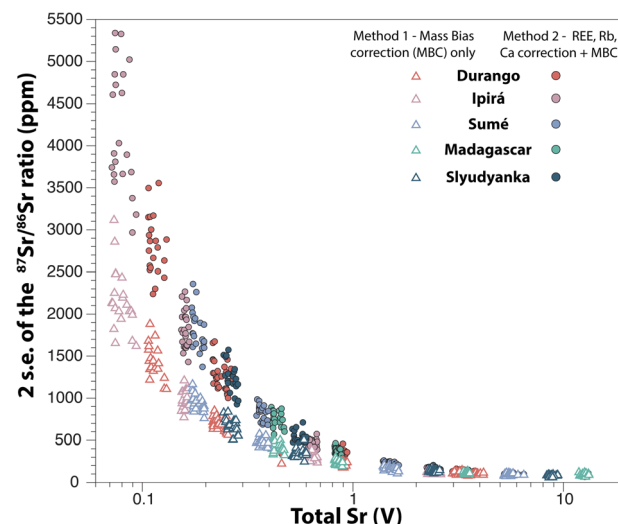


Fig. 10 Precision on the $^{87}\text{Sr}/^{86}\text{Sr}$ ratio (given by the 2 s.e. of individual measurements) as a function of the total Sr intensity and the method used for data reduction.

4. Discussion

4.1. Precision on the $^{87}\text{Sr}/^{86}\text{Sr}$ ratio

The precision on the $^{87}\text{Sr}/^{86}\text{Sr}$ ratio critically depends on the total intensity measured on Sr, as summarised in Fig. 10. An internal precision better than 100 ppm (2 s.e.) is typically achieved for total Sr intensities greater than 8 V, and overall *Method 1* provides more precise data than *Method 2*. The better precision of *Method 1* is explained by the reduced number of data reduction steps compared to *Method 2*, and by the large uncertainty in the measurement of small intensities on half-masses (Fig. 3b and 4).

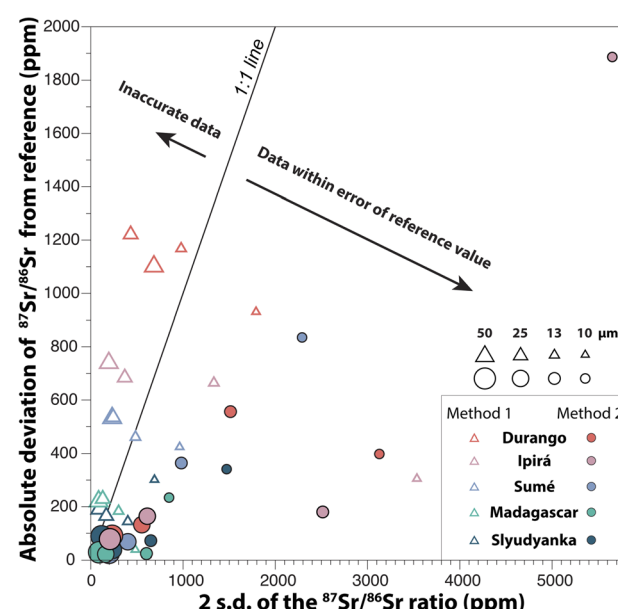


Fig. 11 Changes in the absolute average deviation from the reference $^{87}\text{Sr}/^{86}\text{Sr}$ and in the 2 s.d. of the $^{87}\text{Sr}/^{86}\text{Sr}$ ratio, depending on which apatites are analysed, the size of the laser ablation beam and the method used for data reduction.



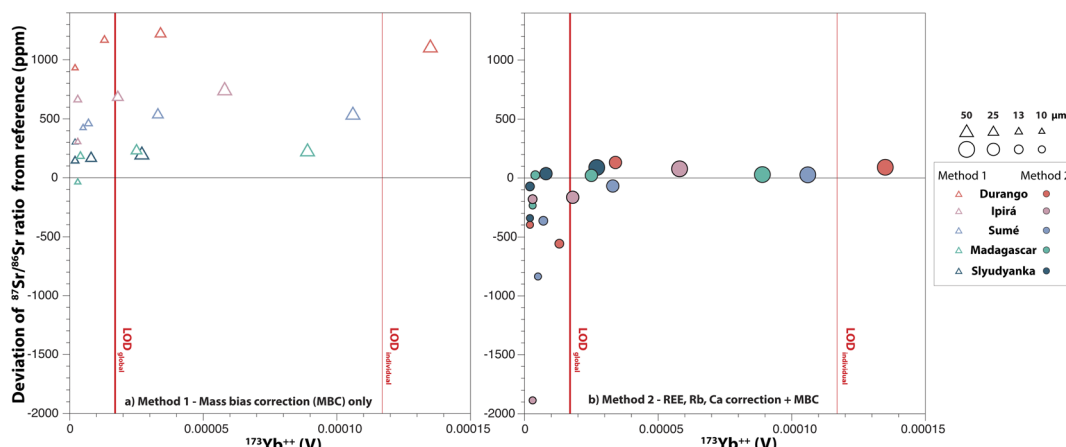


Fig. 12 Average deviation from the reference $^{87}\text{Sr}/^{86}\text{Sr}$ ratio as a function of the $^{173}\text{Yb}^{++}$ intensity measured on m/z 86.5. (a) *Method 1* and (b) *Method 2* for data reduction. Symbols and colour codes are same as in Fig. 11. The $\text{LOD}_{\text{individual}}$ (thin red lines) is the average 3 s.d. of individual gas blank intensities, and the $\text{LOD}_{\text{global}}$ (thick red lines) is the 3 s.d. of 460 gas blank analyses.

4.2. Accuracy and reproducibility of $^{87}\text{Sr}/^{86}\text{Sr}$

The average deviation from the reference $^{87}\text{Sr}/^{86}\text{Sr}$ of the five apatite standards is plotted in Fig. 11 as a function of the external reproducibility (given by the 2 s.d.) of the $^{87}\text{Sr}/^{86}\text{Sr}$ ratios measured at different laser ablation beam sizes. At 50 µm and 25 µm, both methods give similar external reproducibility, and the best 2 s.d. of *c.a.* 100 ppm is obtained in low REE/Sr apatites (*i.e.* Madagascar and Slyudyanka). At smaller laser ablation beam sizes (*i.e.* 13 µm and 10 µm), a better reproducibility of the measurements is achieved with *Method 1*.

The 1:1 line in Fig. 11 separates the data that should be considered within error of the reference value, from data that should not. When *Method 1* is used for data reduction, the accuracy of the measurements is clearly affected for apatites with high REE/Sr ratios, such as Durango, Sumé and Ipirá. Analyses with 50 µm and 25 µm laser ablation beam sizes, which are the most precise in this study (Fig. 10), are significantly shifted from the reference value, by +190 to +1100 ppm (Fig. 11). When *Method 2* is used, the accuracy is greatly improved at 50 µm and 25 µm, although a substantial deviation from the reference value (of up to 2000 ppm) is observed for smaller ablation beams (*i.e.* 13 µm and 10 µm).

4.3. Importance of the limit of detection (LOD)

The average deviation from the reference $^{87}\text{Sr}/^{86}\text{Sr}$ of the five apatite standards is plotted as a function of the $^{173}\text{Yb}^{++}$ intensity measured on m/z 86.5 in Fig. 12. The $\text{LOD}_{\text{individual}}$ and $\text{LOD}_{\text{global}}$, which were previously introduced in Section 3.1. (see Fig. 4), are reported in this figure, and it is striking that all analyses at 10 µm and 13 µm plot well below both the $\text{LOD}_{\text{individual}}$ and $\text{LOD}_{\text{global}}$. At 25 µm, 4 out of 5 apatite standards plot between the lower and upper LOD bounds (*i.e.* $\text{LOD}_{\text{global}}$ and $\text{LOD}_{\text{individual}}$, respectively) with only Slyudyanka plotting below the $\text{LOD}_{\text{global}}$. At 50 µm, all apatites plot above the $\text{LOD}_{\text{global}}$, with only Durango plotting above the $\text{LOD}_{\text{individual}}$.

The information combined from Fig. 11 and 12 indicate that when interfering species are measured below the $\text{LOD}_{\text{global}}$,

Method 1 produces $^{87}\text{Sr}/^{86}\text{Sr}$ ratios with an acceptable level of accuracy. When interfering species are measured near or above the $\text{LOD}_{\text{global}}$, *Method 2* delivers Sr isotope data with an excellent level of accuracy.

4.4. Comparison with previous studies

A number of attempts have been made to measure $^{87}\text{Sr}/^{86}\text{Sr}$ ratios in apatite with a high spatial resolution, as summarised in Fig. 13. Overall, our approach provides a better precision for beam sizes between 50 µm and 10 µm, although a direct comparison with other studies would require a precise estimate of the volume of sample analysed. For instance, the volumes of apatite ablated in this study at 50 µm, 25 µm, 13 µm and 10 µm were around 75 000 µm³, 19 000 µm³, 5000 µm³, and 3000 µm³, respectively.

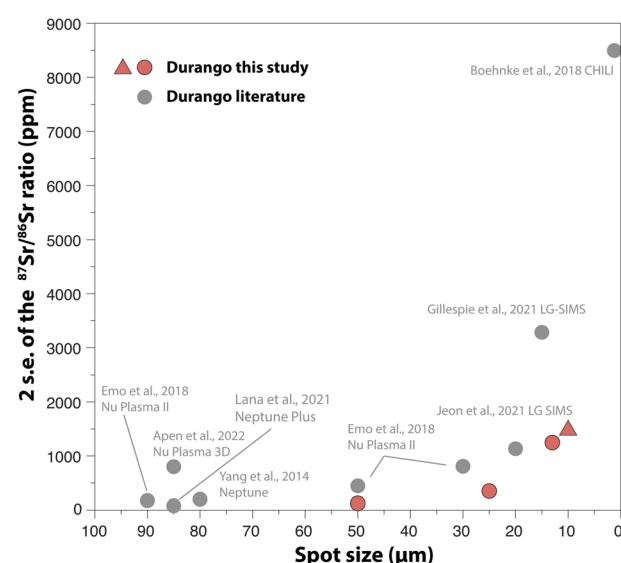


Fig. 13 Precision on the $^{87}\text{Sr}/^{86}\text{Sr}$ ratio measured in Durango apatite with different mass spectrometry techniques. Red symbols: this study (triangles: *Method 1*; circles: *Method 2* for data reduction), and grey circles: literature data.^{24,25,29,67,77,85,86}



Amongst other techniques for high-precision analysis of Sr isotopes, the less destructive nature of the SIMS (Secondary Ion Mass Spectrometry) and CHILI (Chicago instrument for Laser Ionisation;⁸⁴) techniques may be preferred for applications that require analyses of infinitesimal volumes of samples (e.g., <100 μm^3), such as in cosmochemistry. Our new data however demonstrate that LA-MC-ICP-MS platforms that are available in many laboratories worldwide can compete with other *in situ* techniques for Sr isotope measurements through faster acquisition and higher internal precision at comparable spatial resolution.

5. Conclusions and perspectives

The approach developed here allows precise and accurate $^{87}\text{Sr}/^{86}\text{Sr}$ ratios to be obtained when small volumes of apatite are ablated (i.e. 3000 to 75 000 μm^3). Overall, both *Method 1* and *Method 2* for (LA)-MC-ICP-MS data reduction produce $^{87}\text{Sr}/^{86}\text{Sr}$ ratios with good precision and reproducibility. The accuracy of the $^{87}\text{Sr}/^{86}\text{Sr}$ strongly depends on both the composition of the ablated material and the method used for data reduction. As a guidance for method selection, three important points should be considered:

(i) *Method 1* can provide accurate and highly precise Sr isotope data when $^{173}\text{Yb}^{++}$ intensity is measured below the $\text{LOD}_{\text{global}}$.

(ii) *Method 2* greatly improves data accuracy when $^{173}\text{Yb}^{++}$ intensity is measured near or above the $\text{LOD}_{\text{global}}$. However, the uncertainty of individual measurements can be up to two times higher than with *Method 1*.

(iii) Analyses for which $^{173}\text{Yb}^{++}$ intensity is close to the $\text{LOD}_{\text{global}}$ should be treated with caution, and *Method 2* is recommended for more accurate (though less precise) results.

Overall, this analytical protocol for LA-MC-ICP-MS analyses and data reduction can be transposed to a wide range of applications that require a high spatial resolution, including the analysis of minute mineral inclusions, growth zones in rock-forming minerals, and growth zones in carbonates (e.g., shells) and bio-apatite materials (e.g., fish-otoliths, bones, teeth enamel).

Author contributions

A. B. and B. D. designed the study and wrote the first draft of the paper. A. B., H. M. and B. D. performed LA-MC-ICP-MS analyses, and A. B. build data reduction schemes with help of B. D., H. M. and O. B.; D. B. and H. M. did the wet chemistry and O. B. and D. B. performed solution MC-ICP-MS analyses. All authors contributed to writing the final version of the paper.

Conflicts of interest

There are no conflicts to declare.

Acknowledgements

This project was funded by the European Research Council under the European Union's Horizon 2020 research and innovation program (No. 817934). We thank Cristiano Lana for

providing fragments of the Ipirá and Sumé apatites. We thank Emma Stephen for editorial handling, as well as the two anonymous reviewers for their constructive comments and suggestions.

Notes and references

- 1 R. L. Armstrong, A model for the evolution of strontium and lead isotopes in a dynamic Earth, *Rev. Geophys.*, 1968, **6**(2), 175–199.
- 2 D. J. DePaolo, Trace element and isotopic effects of combined wallrock assimilation and fractional crystallization, *Earth Planet. Sci. Lett.*, 1981, **53**(2), 189–202.
- 3 K. M. Frei, U. Mannering, K. Kristiansen, M. E. Allentoft, A. S. Wilson, I. Skals, *et al.*, Tracing the dynamic life story of a Bronze Age Female, *Sci. Rep.*, 2015, **5**(1), 10431.
- 4 J. Montgomery, J. Evans and M. S. A. Horstwood, Evidence for long-term averaging of strontium in bovine enamel using TIMS and LA-MC-ICP-MS strontium isotope intramolar profiles, *Environ. Archaeol.*, 2010, **15**, 32–42.
- 5 F. Lugli, A. Cipriani, C. Peretto, M. Mazzucchelli and D. Brunelli, *In situ* high spatial resolution $^{87}\text{Sr}/^{86}\text{Sr}$ ratio determination of two Middle Pleistocene (c.a. 580 ka) Stephanorhinus hundsheimensis teeth by LA-MC-ICP-MS, *Int. J. Mass Spectrom.*, 2017, **412**, 38–48.
- 6 J. M. McCormack, A. Bahr, A. Gerdes, T. Tütken and P. Prinz-Grimm, Preservation of successive diagenetic stages in Middle Triassic bonebeds: Evidence from *in situ* trace element and strontium isotope analysis of vertebrate fossils, *Chem. Geol.*, 2015, **410**, 108–123.
- 7 C. P. Bataille, B. E. Crowley, M. J. Wooller and G. J. Bowen, Advances in global bioavailable strontium isoscapes, *Palaeogeogr., Palaeoclimatol., Palaeoecol.*, 2020, **555**, 109849.
- 8 C. P. Bataille, S. R. Brennan, J. Hartmann, N. Moosdorf, M. J. Wooller and G. J. Bowen, A geostatistical framework for predicting variations in strontium concentrations and isotope ratios in Alaskan rivers, *Chem. Geol.*, 2014, **389**, 1–15.
- 9 M. J. Bickle, H. J. Chapman, E. Tipper, A. Galy, C. L. De La Rocha and T. Ahmad, Chemical weathering outputs from the flood plain of the Ganga, *Geochim. Cosmochim. Acta*, 2018, **225**, 146–175.
- 10 S. R. Brennan, D. E. Schindler, T. J. Cline, T. E. Walsworth, G. Buck and D. P. Fernandez, Shifting habitat mosaics and fish production across river basins, *Science*, 2019, **364**(6442), 783–786.
- 11 E. C. Chapman, R. C. Capo, B. W. Stewart, C. S. Kirby, R. W. Hammack, K. T. Schroeder, *et al.*, Geochemical and Strontium Isotope Characterization of Produced Waters from Marcellus Shale Natural Gas Extraction, *Environ. Sci. Technol.*, 2012, **46**(6), 3545–3553.
- 12 L. S. Ruhl, G. S. Dwyer, H. Hsu-Kim, J. C. Hower and A. Vengosh, Boron and Strontium Isotopic Characterization of Coal Combustion Residuals: Validation of New Environmental Tracers, *Environ. Sci. Technol.*, 2014, **48**(24), 14790–14798.
- 13 J. D. Vilomet, B. Angeletti, S. Moustier, J. P. Ambrosi, M. Wiesner, J. Y. Bottero, *et al.*, Application of Strontium



- Isotopes for Tracing Landfill Leachate Plumes in Groundwater, *Environ. Sci. Technol.*, 2001, **35**(23), 4675–4679.
- 14 E. J. Bartelink and L. A. Chesson, Recent applications of isotope analysis to forensic anthropology, *Forensic Sci. Prog.*, 2019, **4**(1), 29–44.
- 15 R. T. Kramer, E. J. Bartelink, N. P. Herrmann, C. P. Bataille and K. Spradley, Application of stable isotopes and geostatistics to infer region of geographical origin for deceased undocumented Latin American migrants, In Parra R. C., Zapico S. C. and Ubelaker D. H., eds., *Forensic Science and Humanitarian Action [Internet]*, 1st edn, Wiley, 2020, pp. 425–40, Available from, <https://onlinelibrary.wiley.com/doi/10.1002/9781119482062.ch27>.
- 16 C. Durante, C. Baschieri, L. Bertacchini, M. Cocchi, S. Sighinolfi, M. Silvestri, *et al.*, Geographical traceability based on $^{87}\text{Sr}/^{86}\text{Sr}$ indicator: A first approach for PDO Lambrusco wines from Modena, *Food Chem.*, 2013, **141**(3), 2779–2787.
- 17 S. Marchionni, A. Buccianti, A. Bollati, E. Braschi, F. Cifelli, P. Molin, *et al.*, Conservation of $^{87}\text{Sr}/^{86}\text{Sr}$ isotopic ratios during the winemaking processes of 'Red' wines to validate their use as geographic tracer, *Food Chem.*, 2016, **190**, 777–785.
- 18 S. Marchionni, E. Braschi, S. Tommasini, A. Bollati, F. Cifelli, N. Mulinacci, *et al.*, High-Precision $^{87}\text{Sr}/^{86}\text{Sr}$ Analyses in Wines and Their Use as a Geological Fingerprint for Tracing Geographic Provenance, *J. Agric. Food Chem.*, 2013, **61**(28), 6822–6831.
- 19 S. Rummel, S. Hoelzl, P. Horn, A. Rossmann and C. Schlicht, The combination of stable isotope abundance ratios of H, C, N and S with $^{87}\text{Sr}/^{86}\text{Sr}$ for geographical origin assignment of orange juices, *Food Chem.*, 2010, **118**(4), 890–900.
- 20 S. Voerkelius, G. D. Lorenz, S. Rummel, C. R. Quétel, G. Heiss, M. Baxter, *et al.*, Strontium isotopic signatures of natural mineral waters, the reference to a simple geological map and its potential for authentication of food, *Food Chem.*, 2010, **118**(4), 933–940.
- 21 S. B. Jacobsen and K. S. Heier, Rb-Sr isotope systematics in metamorphic rocks, Kongsberg sector, south Norway, *Lithos*, 1978, **11**(4), 257–276.
- 22 O. Nebel and K. Mezger, Timing of thermal stabilization of the Zimbabwe Craton deduced from high-precision Rb-Sr chronology, Great Dyke, *Precambrian Res.*, 2008, **164**(3–4), 227–232.
- 23 C. Wang, O. Alard, Y. J. Lai, S. F. Foley, Y. Liu, J. Munnikhuys, *et al.*, Advances in in-situ Rb-Sr dating using LA-ICP-MS/MS: applications to igneous rocks of all ages and to the identification of unrecognized metamorphic events, *Chem. Geol.*, 2022, **610**, 121073.
- 24 R. B. Emo, M. A. Smit, M. Schmitt, E. Kooijman, E. E. Scherer, P. Sprung, *et al.*, Evidence for evolved Hadean crust from Sr isotopes in apatite within Eoarchean zircon from the Acosta Gneiss Complex, *Geochim. Cosmochim. Acta*, 2018, **235**, 450–462.
- 25 J. Gillespie, A. A. Nemchin, P. D. Kinny, L. Martin, M. Aleshin, M. P. Roberts, *et al.*, Strontium isotope analysis of apatite via SIMS, *Chem. Geol.*, 2021, **559**, 119979.
- 26 M. S. A. Horstwood, J. A. Evans and J. Montgomery, Determination of Sr isotopes in calcium phosphates using laser ablation inductively coupled plasma mass spectrometry and their application to archaeological tooth enamel, *Geochim. Cosmochim. Acta*, 2008, **72**(23), 5659–5674.
- 27 F. Lugli, M. Weber, T. Giovanardi, S. Arrighi, E. Bortolini, C. Figus, *et al.*, Fast offline data reduction of laser ablation MC-ICP-MS Sr isotope measurements via an interactive Excel-based spreadsheet 'SrDR', *J. Anal. At. Spectrom.*, 2020, **35**(5), 852–862.
- 28 W. Müller and R. Anczkiewicz, Accuracy of laser-ablation (LA)-MC-ICPMS Sr isotope analysis of (bio)apatite – a problem reassessed, *J. Anal. At. Spectrom.*, 2016, **31**(1), 259–269.
- 29 Y. H. Yang, F. Y. Wu, J. H. Yang, D. M. Chew, L. W. Xie, Z. Y. Chu, *et al.*, Sr and Nd isotopic compositions of apatite reference materials used in U-Th-Pb geochronology, *Chem. Geol.*, 2014, **385**, 35–55.
- 30 M. Cao, P. Hollings, N. J. Evans, D. R. Cooke, B. I. A. McInnes, K. Zhao, *et al.*, In Situ Elemental and Sr Isotope Characteristics of Magmatic to Hydrothermal Minerals from the Black Mountain Porphyry Deposit, Baguio District, Philippines, *Econ. Geol.*, 2020, **115**(4), 927–944.
- 31 M. A. Edwards, M. G. Jackson, A. R. C. Kylander-Clark, J. Harvey, G. A. Hagen-Peter, G. G. E. Seward, *et al.*, Extreme enriched and heterogeneous $^{87}\text{Sr}/^{86}\text{Sr}$ ratios recorded in magmatic plagioclase from the Samoan hotspot, *Earth Planet. Sci. Lett.*, 2019, **511**, 190–201.
- 32 G. Hagen-Peter, C. Tegner and C. E. Lesher, Strontium isotope systematics for plagioclase of the Skaergaard intrusion (East Greenland): A window to crustal assimilation, differentiation, and magma dynamics, *Geology*, 2019, **47**(4), 313–316.
- 33 J. I. Kimura, T. Takahashi and Q. Chang, A new analytical bias correction for *in situ* Sr isotope analysis of plagioclase crystals using laser-ablation multiple-collector inductively coupled plasma mass spectrometry, *J. Anal. At. Spectrom.*, 2013, **28**(6), 945–957.
- 34 L. Gorojovsky and O. Alard, Optimisation of laser and mass spectrometer parameters for the *in situ* analysis of Rb/Sr ratios by LA-ICP-MS/MS, *J. Anal. At. Spectrom.*, 2020, **35**(10), 2322–2336.
- 35 D. L. Burgin, J. M. Scott, P. J. le Roux, G. Howarth, M. C. Palmer, T. A. Czertowicz, *et al.*, Rapid characterisation of Mars' mantle reservoirs by *in situ* laser ablation $^{87}\text{Sr}/^{86}\text{Sr}$ analysis of shocked feldspar (maskelynite), *Geochim. Cosmochim. Acta*, 2023, **341**, 46–61.
- 36 C. Hawkesworth, J. Marsh, A. Duncan, A. Erlank and M. Norry, The role of continental lithosphere in the generation of the Karoo volcanic rocks: evidence from combined Nd-and Sr-isotopes studies, *Geol. Soc. S. Afr., Spec. Publ.*, 1984, **13**, 341–354.



- 37 M. Martelli, P. Nuccio, F. Stuart, R. Burgess, R. Ellam and F. Italiano, Helium–strontium isotope constraints on mantle evolution beneath the Roman Comagmatic Province, Italy, *Earth Planet. Sci. Lett.*, 2004, **224**(3–4), 295–308.
- 38 A. Rosenthal, S. Foley, D. G. Pearson, G. M. Nowell and S. Tappe, Petrogenesis of strongly alkaline primitive volcanic rocks at the propagating tip of the western branch of the East African Rift, *Earth Planet. Sci. Lett.*, 2009, **284**(1–2), 236–248.
- 39 H. P. Taylor Jr, The effects of assimilation of country rocks by magmas on $^{18}\text{O}/^{16}\text{O}$ and $^{87}\text{Sr}/^{86}\text{Sr}$ systematics in igneous rocks, *Earth Planet. Sci. Lett.*, 1980, **47**(2), 243–254.
- 40 Z. F. Zhao, L. Q. Dai and Y. F. Zheng, Postcollisional mafic igneous rocks record crust–mantle interaction during continental deep subduction, *Sci. Rep.*, 2013, **3**(1), 3413.
- 41 E. Braschi, F. Mastroianni, S. Di Salvo, M. Casalini, S. Agostini, G. Vougioukalakis, *et al.*, Unveiling the occurrence of transient, multi-contaminated mafic magmas inside a rhyolitic reservoir feeding an explosive eruption (Nisyros, Greece), *Lithos*, 2022, **410**, 106574.
- 42 S. Di Salvo, E. Braschi, M. Casalini, S. Marchionni, T. Adani, M. Uliivi, *et al.*, High-Precision *In Situ* $^{87}\text{Sr}/^{86}\text{Sr}$ Analyses through Microsampling on Solid Samples: Applications to Earth and Life Sciences. Termopoli V, editor, *J. Anal. Methods Chem.*, 2018, **2018**, 1292954.
- 43 L. Francalanci, R. Avanzinelli, I. Nardini, M. Tiepolo, J. P. Davidson and R. Vannucci, Crystal recycling in the steady-state system of the active Stromboli volcano: a 2.5-ka story inferred from *in situ* Sr-isotope and trace element data, *Contrib. Mineral. Petrol.*, 2012, **163**(1), 109–131.
- 44 S. Jung, J. Pfänder, M. Brauns and R. Maas, Crustal contamination and mantle source characteristics in continental intra-plate volcanic rocks: Pb, Hf and Os isotopes from central European volcanic province basalts, *Geochim. Cosmochim. Acta*, 2011, **75**(10), 2664–2683.
- 45 M. Mamani, G. Wörner and T. Sempere, Geochemical variations in igneous rocks of the Central Andean orocline (13 S to 18 S): Tracing crustal thickening and magma generation through time and space, *Bulletin*, 2010, **122**(1–2), 162–182.
- 46 M. Yamamoto, H. Kagami, A. Narita, T. Maruyama, A. Kondo, S. Abe, *et al.*, Sr and Nd isotopic compositions of mafic xenoliths and volcanic rocks from the Oga Peninsula, Northeast Japan Arc: Genetic relationship between lower crust and arc magmas, *Lithos*, 2013, **162**, 88–106.
- 47 C. J. Allègre, S. R. Hart and J. F. Minster, Chemical structure and evolution of the mantle and continents determined by inversion of Nd and Sr isotopic data, I. Theoretical methods, *Earth Planet. Sci. Lett.*, 1983, **66**, 177–190.
- 48 B. Dhuime, A. Wuestefeld and C. J. Hawkesworth, Emergence of modern continental crust about 3 billion years ago, *Nat. Geosci.*, 2015, **8**(7), 552–555.
- 49 M. T. McCulloch and G. J. Wasserburg, Sm-Nd and Rb-Sr Chronology of Continental Crust Formation: Times of addition to continents of chemically fractionated mantle-derived materials are determined, *Science*, 1978, **200**(4345), 1003–1011.
- 50 J. Veizer and W. Compston, $^{87}\text{Sr}/^{86}\text{Sr}$ in Precambrian carbonates as an index of crustal evolution, *Geochim. Cosmochim. Acta*, 1976, **40**(8), 905–914.
- 51 A. Krabbenhöft, J. Fietzke, A. Eisenhauer, V. Liebetrau, F. Böhm and H. Vollstaedt, Determination of radiogenic and stable strontium isotope ratios ($^{87}\text{Sr}/^{86}\text{Sr}$; $\delta^{88}/^{86}\text{Sr}$) by thermal ionization mass spectrometry applying an $^{87}\text{Sr}/^{84}\text{Sr}$ double spike, *J. Anal. At. Spectrom.*, 2009, **24**(9), 1267.
- 52 P. Montero and F. Bea, Accurate determination of $^{87}\text{Rb}/^{86}\text{Sr}$ and $^{147}\text{Sm}/^{144}\text{Nd}$ ratios by inductively-coupled-plasma mass spectrometry in isotope geoscience: an alternative to isotope dilution analysis, *Anal. Chim. Acta*, 1998, **358**(3), 227–233.
- 53 E. Yobregat, C. Fitoussi and B. Bourdon, A new method for TIMS high precision analysis of Ba and Sr isotopes for cosmochemical studies, *J. Anal. At. Spectrom.*, 2017, **32**(7), 1388–1399.
- 54 M. Bizzarro, A. Simonetti, R. K. Stevenson and S. Kurszlaukis, *In situ* $^{87}\text{Sr}/^{86}\text{Sr}$ investigation of igneous apatites and carbonates using laser-ablation MC-ICP-MS, *Geochim. Cosmochim. Acta*, 2003, **67**(2), 289–302.
- 55 A. Lepland and M. J. Whitehouse, Metamorphic alteration, mineral paragenesis and geochemical re-equilibration of early Archean quartz–amphibole–pyroxene gneiss from Akilia, Southwest Greenland, *Int. J. Earth Sci.*, 2011, **100**(1), 1–22.
- 56 F. C. Ramos, J. A. Wolff and D. L. Tollstrup, Measuring $^{87}\text{Sr}/^{86}\text{Sr}$ variations in minerals and groundmass from basalts using LA-MC-ICPMS, *Chem. Geol.*, 2004, **211**(1–2), 135–158.
- 57 J. Irrgeher, P. Galler and T. Prohaska, $^{87}\text{Sr}/^{86}\text{Sr}$ isotope ratio measurements by laser ablation multicollector inductively coupled plasma mass spectrometry: Reconsidering matrix interferences in bioapatites and biogenic carbonates, *Spectrochim. Acta, Part B*, 2016, **125**, 31–42.
- 58 M. Jackson and S. Hart, Strontium isotopes in melt inclusions from Samoan basalts: Implications for heterogeneity in the Samoan plume, *Earth Planet. Sci. Lett.*, 2006, **245**(1–2), 260–277.
- 59 J. Mulder, G. Hagen-Peter, T. Ubide, R. Andreasen, E. Kooijman, M. Kielman-Schmitt, *et al.*, New Reference Materials, Analytical Procedures and Data Reduction Strategies for Sr Isotope Measurements in Geological Materials by LA-MC-ICP-MS, *Geostand. Geoanal. Res.*, 2023, ggr.12480.
- 60 P. Z. Vroon, B. van der Wagt, J. M. Koornneef and G. R. Davies, Problems in obtaining precise and accurate Sr isotope analysis from geological materials using laser ablation MC-ICPMS, *Anal. Bioanal. Chem.*, 2008, **390**(2), 465–476.
- 61 Z. Yang, B. J. Fryer, H. P. Longerich, J. E. Gagnon and I. M. Samson, 785 nm femtosecond laser ablation for improved precision and reduction of interferences in Sr isotope analyses using MC-ICP-MS, *J. Anal. At. Spectrom.*, 2011, **26**(2), 341–351.



- 62 D. M. Chew, J. A. Petrus and B. S. Kamber, U-Pb LA-ICPMS dating using accessory mineral standards with variable common Pb, *Chem. Geol.*, 2014, **363**, 185–199.
- 63 D. M. Chew, P. J. Sylvester and M. N. Tubrett, U-Pb and Th-Pb dating of apatite by LA-ICPMS, *Chem. Geol.*, 2011, **280**(1–2), 200–216.
- 64 C. L. Kirkland, C. Yakymchuk, K. Szilas, N. Evans, J. Hollis, B. McDonald, *et al.*, Apatite: a U-Pb thermochronometer or geochronometer?, *Lithos*, 2018, **318–319**, 143–157.
- 65 O. Laurent, A. Zeh, A. Gerdes, A. Villaros, K. Gros and E. Slaby, How do granitoid magmas mix with each other? Insights from textures, trace element and Sr-Nd isotopic composition of apatite and titanite from the Matok pluton (South Africa), *Contrib. Mineral. Petrol.*, 2017, **172**(9), 80.
- 66 X. C. Li, D. E. Harlov, M. F. Zhou and H. Hu, Metasomatic modification of Sr isotopes in apatite as a function of fluid chemistry, *Geochim. Cosmochim. Acta*, 2022, **323**, 123–140.
- 67 P. Boehnke, E. A. Bell, T. Stephan, R. Trappitsch, C. B. Keller, O. S. Pardo, *et al.*, Potassic, high-silica Hadean crust, *Proc. Natl. Acad. Sci. U. S. A.*, 2018, **115**(25), 6353–6356.
- 68 B. Dhuime, J. Lewis, E. Bruand and C. Hawkesworth, New insights into crustal evolution studies from Sr isotopes, *EGU General Assembly Conference Abstracts*, 2014, p. 4173.
- 69 J. Gillespie, P. D. Kinny, C. L. Kirkland, L. Martin, A. A. Nemchin, A. J. Cavosie, *et al.*, Isotopic modelling of Archean crustal evolution from comagmatic zircon–apatite pairs, *Earth Planet. Sci. Lett.*, 2021, **575**, 117194.
- 70 Y. H. Yang, F. Y. Wu, L. W. Xie, Z. Y. Chu and J. H. Yang, Re-evaluation of interferences of doubly charged ions of heavy rare earth elements on Sr isotopic analysis using multi-collector inductively coupled plasma mass spectrometry, *Spectrochim. Acta, Part B*, 2014, **97**, 118–123.
- 71 G. L. Foster and D. Vance, In situ Nd isotopic analysis of geological materials by laser ablation MC-ICP-MS, *J. Anal. At. Spectrom.*, 2006, **21**(3), 288.
- 72 J. Lewis, C. D. Coath and A. W. G. Pike, An improved protocol for $^{87}\text{Sr}/^{86}\text{Sr}$ by laser ablation multi-collector inductively coupled plasma mass spectrometry using oxide reduction and a customised plasma interface, *Chem. Geol.*, 2014, **390**, 173–181.
- 73 T. Waight, J. Baker and D. Peate, Sr isotope ratio measurements by double-focusing MC-ICPMS: techniques, observations and pitfalls, *Int. J. Mass Spectrom.*, 2002, **221**(3), 229–244.
- 74 J. Woodhead, S. Swearer, J. Hergt and R. Maas, In situ Sr-isotope analysis of carbonates by LA-MC-ICP-MS: interference corrections, high spatial resolution and an example from otolith studies, *J. Anal. At. Spectrom.*, 2005, **20**(1), 22.
- 75 A. N. Paul, R. A. Spikings and S. P. Gaynor, U-Pb ID-TIMS reference ages and initial Pb isotope compositions for Durango and Wilberforce apatites, *Chem. Geol.*, 2021, **586**, 120604.
- 76 S. N. Thomson, G. E. Gehrels, J. Ruiz and R. Buchwaldt, Routine low-damage apatite U-Pb dating using laser ablation–multicollector–ICPMS, *Geochem., Geophys., Geosyst.*, 2012, **13**(2), 1–23.
- 77 C. Lana, G. O. Gonçalves, A. Mazoz, I. Buick, S. Kamo, R. Scholz, *et al.*, Assessing the U-Pb, Sm-Nd and Sr-Sr Isotopic Compositions of the Sumé Apatite as a Reference Material for LA-ICP-MS Analysis, *Geostand. Geoanal. Res.*, 2022, **46**(1), 71–95.
- 78 C. Pin, D. Briot, C. Bassin and F. Poitrasson, Concomitant separation of strontium and samarium-neodymium for isotopic analysis in silicate samples, based on specific extraction chromatography, *Anal. Chim. Acta*, 1994, **298**(2), 209–217.
- 79 C. Huang, Y. H. Yang, J. H. Yang and L. W. Xie, In situ simultaneous measurement of Rb-Sr/Sm-Nd or Sm-Nd/Lu-Hf isotopes in natural minerals using laser ablation multi-collector ICP-MS, *J. Anal. At. Spectrom.*, 2015, **30**(4), 994–1000.
- 80 M. Alba, F. Tanner De Oliveira and G. Paolo Sighinolfi, Geochemistry of Precambrian phosphate-carbonate intrusives from Bahia (Brazil), *Geochem. J.*, 1983, **17**(6), 277–287.
- 81 W. Müller, M. Shelley, P. Miller and S. Broude, Initial performance metrics of a new custom-designed ArF excimer LA-ICPMS system coupled to a two-volume laser-ablation cell, *J. Anal. At. Spectrom.*, 2009, **24**(2), 209–214.
- 82 G. Craig, A. J. Managh, C. Stremtan, N. S. Lloyd and M. S. A. Horstwood, Doubling Sensitivity in Multicollector ICPMS Using High-Efficiency, Rapid Response Laser Ablation Technology, *Anal. Chem.*, 2018, **90**(19), 11564–11571.
- 83 K. J. R. Rosman and P. D. P. Taylor, Isotopic compositions of the elements 1997 (Technical Report), *Pure Appl. Chem.*, 1998, **70**(1), 217–235.
- 84 T. Stephan, R. Trappitsch, A. M. Davis, M. J. Pellin, D. Rost, M. R. Savina, *et al.*, CHILI – the Chicago Instrument for Laser Ionization – a new tool for isotope measurements in cosmochemistry, *Int. J. Mass Spectrom.*, 2016, **407**, 1–15.
- 85 F. E. Apen, C. J. Wall, J. M. Cottle, M. D. Schmitz, A. R. C. Kylander-Clark and G. E. Seward, Apatites for destruction: Reference apatites from Morocco and Brazil for U-Pb petrochronology and Nd and Sr isotope geochemistry, *Chem. Geol.*, 2022, **590**, 1–16.
- 86 H. Jeon and M. J. Whitehouse, A Robust LG-SIMS Method for Sr Isotope Determination in Apatite Across a Wide Sr Concentration Range, *Geostand. Geoanal. Res.*, 2021, **45**(2), 325–340.

